Chinese Journal of Aeronautics, (2023), 36(9): 207–220

Chinese Society of Aeronautics and Astronautics
& Beihang University

Chinese Journal of Aeronautics

cja@buaa.edu.cn
www.sciencedirect.com

Influence of differential longitudinal cyclic pitch on flight dynamics of coaxial compound helicopter

Yanqin ZHAO [a], Ye YUAN [b], Renliang CHEN [a,*]

[a] National Key Laboratory of Helicopter Aeromechanics, Nanjing University of Aeronautics and Astronautics, Nanjing 210016, China
[b] Department of Aerospace Engineering, Swansea University, Swansea city SA1 8EN, UK

Received 1 September 2022; revised 20 October 2022; accepted 17 December 2022
Available online 8 June 2023

KEYWORDS

Blade element momentum theory;
Coaxial compound helicopter;
Differential longitudinal cyclic pitch;
Interaction model;
Tip clearance

Abstract The Differential Longitudinal Cyclic Pitch (DLCP) in coaxial compound helicopter is found to be useful in mitigating low-speed rotor interactions and improving flight performance. The complex mutual interaction is simulated by a revised rotor aerodynamics model, where an improved Blade Element Momentum Theory (BEMT) is proposed. Comparisons with the rotor inflow distributions and aircraft trim results from literature validate the accuracy of the model. Then, the influence of the DLCP on the flight dynamics of the aircraft is analysed. The trim characteristics indicate that a negative DLCP can reduce collective and differential collective inputs in low speed forward flight, and the negative longitudinal gradient is alleviated. Moreover, a moderate DLCP can reduce the rotor and total power consumption by 4.68% and 2.9%, respectively. As DLCP further increases, the increased propeller power and unbalanced thrust allocation offset the improvement. In high-speed flight, DLCP does not improve the performance except for extra lateral and heading stick displacements. In addition, the tip clearance is degraded throughout the speed envelope due to the differential pitching moment and the higher thrust from the lower rotor. Meanwhile, the changed rotor efficiency and induced velocity alter low-speed dynamic stability and controllability. The pitch and roll subsidences are slightly degraded with the DLCP, while the heave subsidence, dutch roll and phugoid modes are improved. Lastly, the on-axis controllability, including collective, differential collective pitch, longitudinal and lateral cyclic pitches, varies with DLCP due to its effect on rotor efficiency and inflow distribution. In conclusion, a reasonable DLCP is recommended to adjust the rotor interaction and improve aircraft performance, and further to alter the flight dynamics and aerodynamics of aircraft.

1. Introduction

The coaxial compound helicopter has experienced a lot of interest in recent years due to its high-speed capability. The two rotors inevitably introduce high mutual interference at low speeds. Meanwhile, a total of six controls are available from the coaxial rotor system, and the differential lateral and longitudinal cyclic pitches can be seen as additional control inputs. The differential lateral cyclic pitch has been the hot research point due to its ability in improving the high-speed performance.[1,2] It moves the lift centre toward the

* Corresponding author.
E-mail address: crlae@nuaa.edu.cn (R. CHEN).

https://doi.org/10.1016/j.cja.2023.06.002

advancing side for maximum lift/drag ratio and offloads the retreating side for stall avoidance.

To date, the Differential Longitudinal Cyclic Pitch (DLCP) is usually not considered in engineering and academic researches.[3–5] In the coaxial compound helicopter XH-59A,[6,7] X2 Technology Demonstrator (X2TD)[8,9] and S-97,[10,11] the DLCP was set as 0. In academic researches, the differential longitudinal pitch was also set as 0[3–5] or slightly adjusted to reduce the rotor noise.[12]

Nevertheless, there is a possibility of improving the flight performance by introducing the DLCP to alter low-speed interference. In the coaxial hingeless rotor, a close space between coaxial rotors is designed to reduce the large parasite drag of hubs and inter-rotor shaft.[13] As a result, the interference leads to strong pitching moments as the upper rotor downwash moves to the lower-rotor aft region.[14] On the other hand, the DLCP alters the pitching moment distribution inside the coaxial rotor system, and this moment distribution is the critical factor for the rotor wake shape.[15] Therefore, we wonder if the DLCP can alleviate aerodynamic loads and improve power performance.

However, the flight test of XH59A[6] is the only public document that studied the influence of DLCP on the trim states and stress at speeds over 120 kt (1 kt = 1.852 km/h). The results indicated that the DLCP introduced no significant parameter changes except additional lateral cyclic displacement. To date, no research has studied the effect of DLCP on lower-speed interference and performance, which is the key purpose of this paper.

In order to research the influence of DLCP, a suitable coaxial rotor interaction model is required for interference simulation. Although vortex-wake-based methods[14,16,17] are well-developed, they are mainly used for aerodynamics and aero-acoustics analysis. For preliminary analysis of rotorcraft flight dynamics and performance, the Blade Element Momentum Theory (BEMT),[1,18–20] a fast numerical method, is preferred. Valkov[18] developed the interaction model based on Biot-Savart law. However, the harmonic inflow was obtained based on an empirical function acquired from single-rotor features, resulting in hub-moment underestimation. Leishman and Ananthan[19] developed BEMT for calculating the performance of coaxial proprotor, where only axial motion was considered. Johnson,[1] Lee[20] and Kong[21] developed the momentum theory for coaxial rotors based on fluid mass, momentum, and energy conservation, but their methods need complex and extensive iterations when performing. Therefore, an advanced inflow model is proposed for fast aerodynamics analysis of axial and forward flight.

In light of the preceding discussion, the influence of DLCP on the flight dynamics of the coaxial compound helicopter is investigated. Firstly, a mathematical model is developed and validated, with the rotors modelled by the revised BEMT. Then the trim characteristics of this vehicle at different advance ratio are studied, including stick movements, power consumption and tip clearance. Following this, the dynamic stability variations resulting from the DLCP are assessed, including the longitudinal and lateral/heading stability modes. Lastly, the on-axis controllability of the aircraft at low speeds with strong interference are investigated.

2. Aircraft flight dynamics model

A schematic diagram of the coaxial compound helicopter is given in Fig. 1. The aircraft dynamics model consists of five parts: rotor system, propeller, fuselage, and two empennage surfaces. Among them, the mutual interference between the coaxial rotors makes the flight dynamics model more complex than that of a conventional helicopter. Thus, an advanced blade element momentum theory is developed to simulate the rotor aerodynamics.

2.1. Advanced coaxial rotor aerodynamic model

The coaxial rotor system with airflow interference is the most critical and complex aerodynamic model in the coaxial compound helicopter. The flow field interaction generated from rotor wakes vary with flight speed, resulting in highly nonuniform airflow distribution on rotor disks. Fig. 2 presents the mutual inflow interaction when the two rotors plunged into each other's wake. The direct way to simulate the interaction is by assuming mutual transposition of the induced velocities on blade elements. Therefore, a combined blade element momentum equation is developed.

The normal inflow distribution along the rotor azimuth and span is assumed as

$$\begin{cases} \lambda_{\mathrm{u}}(\bar{r},\psi_{\mathrm{u}}) = v_{i\mathrm{u}}(\bar{r},\psi_{\mathrm{u}}) + v_{i\mathrm{ul}}(\bar{r},\psi_{\mathrm{u}}) + \lambda_0 \\ \lambda_{\mathrm{l}}(\bar{r},\psi_{\mathrm{l}}) = v_{i\mathrm{l}}(\bar{r},\psi_{\mathrm{l}}) + v_{i\mathrm{lu}}(\bar{r},\psi_{\mathrm{l}}) + \lambda_0 \end{cases} \tag{1}$$

which consists of the non-dimensional self-induced velocity ($v_{i\mathrm{u}}$ and $v_{i\mathrm{l}}$), aerodynamic interference from the partner ($v_{i\mathrm{ul}}$ and $v_{i\mathrm{lu}}$), and free airflow in airframe motion (λ_0). In other words, the interference from the other rotor is assumed as the equivalent climb velocity.[22] Local azimuths, ψ_{u} and ψ_{l}, are defined in respective direction of rotor rotations (counterclockwise for the upper rotor from the top view).

The self-induced velocity of each rotor is assumed to be linearly distributed along the span:

$$\begin{cases} v_{i\mathrm{u}}(\bar{r},\psi_{\mathrm{u}}) = v_{i0,\mathrm{u}} + \bar{r}\, v_{is,\mathrm{u}} \sin\psi_{\mathrm{u}} + \bar{r}\, v_{ic,\mathrm{u}} \cos\psi_{\mathrm{u}} \\ v_{i\mathrm{l}}(\bar{r},\psi_{\mathrm{l}}) = v_{i0,\mathrm{l}} + \bar{r}\, v_{is,\mathrm{l}} \sin\psi_{\mathrm{l}} + \bar{r}\, v_{ic,\mathrm{l}} \cos\psi_{\mathrm{l}} \end{cases} \tag{2}$$

The Pitt-Peters dynamic inflow method[23] is applied to calculate the harmonics. Adapted to the coaxial case, it yields

$$\begin{bmatrix} \boldsymbol{M}_{\mathrm{u}} & 0 \\ 0 & \boldsymbol{M}_{\mathrm{l}} \end{bmatrix} \begin{bmatrix} \dot{\boldsymbol{v}}'_{i\mathrm{u}} \\ \dot{\boldsymbol{v}}'_{i\mathrm{l}} \end{bmatrix} + \begin{bmatrix} \boldsymbol{V}_{\mathrm{u}} & 0 \\ 0 & \boldsymbol{V}_{\mathrm{l}} \end{bmatrix} \begin{bmatrix} \boldsymbol{L}_{\mathrm{u}} & 0 \\ 0 & \boldsymbol{L}_{\mathrm{l}} \end{bmatrix}^{-1} \begin{bmatrix} \boldsymbol{v}'_{i\mathrm{u}} \\ \boldsymbol{v}'_{i\mathrm{l}} \end{bmatrix} = \begin{bmatrix} \boldsymbol{\tau}'_{\mathrm{u}} \\ \boldsymbol{\tau}'_{\mathrm{l}} \end{bmatrix} \tag{3}$$

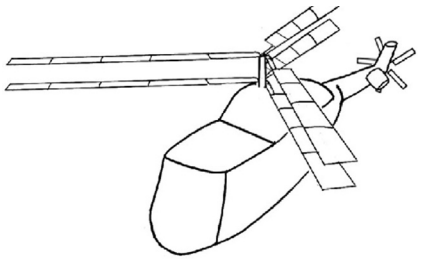

Fig. 1 Schematic diagram of coaxial compound helicopter.

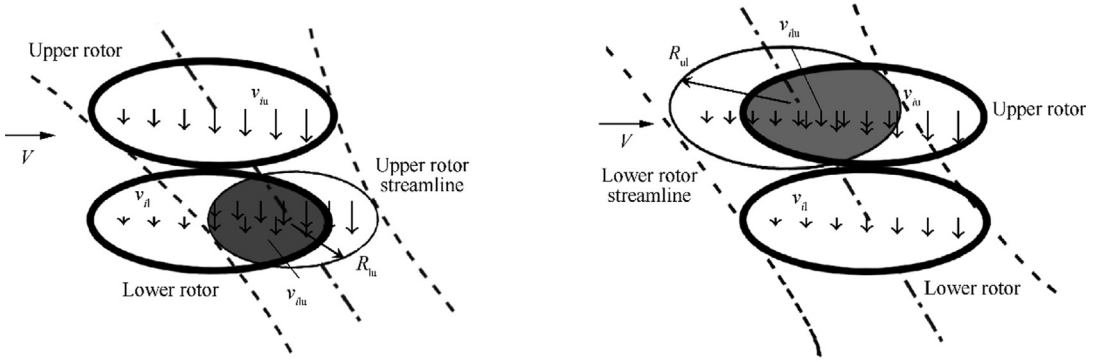

(a) Upper rotor wake interferes with lower rotor

(b) Lower rotor wake interferes with upper rotor

Fig. 2 Wake superposition in forward flight.

where $\boldsymbol{v}_i' = [v_{i0}, v_{is}', v_{ic}']^{\mathrm{T}}$ refers to the self-induced inflow, $\boldsymbol{\tau}' = [C_T', C_{LA}', C_{MA}']^{\mathrm{T}}$ are defined in the rotor hub-wind axis system, and $\boldsymbol{M}, \boldsymbol{V}, \boldsymbol{L}$ are defined in the dynamic inflow equation.[23]

Then, the additional downwash on each rotor can be expressed according to the velocity induced by its partner. Two different streamline models are applied to the coaxial rotors according to their positions relative to the partner. As shown in Fig. 2, the upper rotor is above the slipstream of the lower rotor, resulting in an equivalent climb rate, $v_{i0,\mathrm{ul}}$, lower than the induced velocity $v_{i0,\mathrm{l}}$. The speed ratio, $v_{i0,\mathrm{ul}}/v_{i0,\mathrm{l}}$ is denoted as $\delta_{\mathrm{ul}}(\delta_{\mathrm{ul}} < 1)$. Conversely, the lower rotor is in the contracted wake of the upper rotor, and the inflow from the upper rotor ($v_{i0,\mathrm{lu}}$) increases as reaching the lower rotor. The speed ratio δ_{lu} ($v_{i0,\mathrm{lu}}/v_{i0,\mathrm{u}}$) is higher than unity.

Apart from the airflow speed variation, the actual interference is affected by the overlapped area.[24] In an ideal hover state, if it is assumed that the wake contraction of the upper rotor is not affected, the lower rotor will have one-half of the disk area operating in the upper rotor slipstream.[20] As speed increases, the overlapped area moves rearward and reduces progressively, resulting in varying aerodynamic interference.

The interference on the upper rotor is usually not considered with the assumption of a large space between coaxial rotors.[19,22] In the coaxial compound helicopter, a close distance between rotors is designed for low drag from the hub and shaft.[25] As a result, the interference cannot be ignored.

Here, the Biot-Savart law is applied to simulate the streamline of the lower rotor, which is assumed to be not affected by the upper rotor. Then, the speed ratio regarding the interference acting on the upper rotor is yielded as[18]

$$\delta_{\mathrm{ul}} = \frac{v_{i0,\mathrm{ul}}}{v_{i0,\mathrm{l}}} = 1 + \frac{-D_{\mathrm{lu}}}{\sqrt{R^2\cos^2\chi + D_{\mathrm{lu}}^2}} \tag{4}$$

Then, the wake geometry has the radius

$$R_{\mathrm{ul}} = R/\sqrt{\delta_{\mathrm{ul}}} \tag{5}$$

based on mass conservation, bigger than the rotor disk. Therefore, at extremely low speeds, hover for instance, the overlapped area covers the entire disk of the upper rotor. As speed increases, the induced velocity decreases, and the interference zone washes out gradually. To simulate the interaction without increasing computation complexity, the overlapped area is assumed to cover the entire rotor disk, and is modified by the coefficient γ_{ul}.[18] Thus, the inflow interaction on the upper rotor is yielded as

$$v_{i\mathrm{ul}}(\bar{r}, \psi_{\mathrm{u}}) = \delta_{\mathrm{ul}}\gamma_{\mathrm{ul}}\left(v_{i0,\mathrm{l}} - \bar{r}\, v_{is,\mathrm{l}}\sin\psi_{\mathrm{u}} + \bar{r}\, v_{ic,\mathrm{l}}\cos\psi_{\mathrm{u}}\right) \tag{6}$$

where the transition from the left-hand system (the lower rotor) to the right-hand (the upper rotor) is considered.

The strong interference upon the lower rotor is essential in the coaxial rotor aerodynamic model. A precise model with high fidelity is required. Therefore, the wake properties of the upper rotor are derived by considering helical tip vortex filaments. According to Ref. 26, the streamline vortex at the blade tip can be expressed as

$$\frac{z_w}{R} = \begin{cases} k_1\psi_{\mathrm{w}}, \text{ for } 0 \leqslant \psi_{\mathrm{w}} \leqslant \frac{2\pi}{N_{\mathrm{b}}} \\ \left(\frac{z_{\mathrm{w}}}{R}\right)_{\psi_{\mathrm{w}}=\frac{2\pi}{N_{\mathrm{b}}}} + k_2\left(\psi_{\mathrm{w}} - \frac{2\pi}{N_{\mathrm{b}}}\right), \text{ for } \psi_{\mathrm{w}} \geqslant \frac{2\pi}{N_{\mathrm{b}}} \end{cases} \tag{7}$$

where

$$\begin{cases} k_1 = 0.25(C_T/\sigma + 0.0573\theta_{\mathrm{t}}) \\ k_2 = (1.41 + 0.8079\theta_{\mathrm{t}})\sqrt{C_T/2} \end{cases}$$

ψ_{w} is the wake azimuth angle relative to blade, θ_{t} is the blade twist, σ is the rotor solidity, and N_{b} is the number of the rotor blade.

Then, the vortex radius for a given ψ_{w} is

$$R_{\mathrm{lu}} = 0.78 + 0.22\mathrm{e}^{-(0.145+0.27C_T)\psi_{\mathrm{w}}} \tag{8}$$

where wake-blade interactions and local viscous effects are considered.

The radius contraction ratio is

$$\gamma_{\mathrm{lu}} = R_{\mathrm{lu}}/R \tag{9}$$

As aircraft flies forward, the in-plane velocity component tilts the wake, and places the interaction backwards. Thus, a combination of contraction and translation now determines the streamline shape. The equation for the streamline issued from $(x_{\mathrm{u}}, y_{\mathrm{u}})$ on the upper rotor to the lower rotor is

$$\begin{cases} x_{\mathrm{l}} = \gamma_{\mathrm{lu}}x_{\mathrm{u}} - D_{\mathrm{ul}}\frac{2\mu}{\lambda_{\mathrm{u}}+\lambda_{\mathrm{l}}}\cos\beta_{\mathrm{W,u}} = \gamma_{\mathrm{lu}}x_{\mathrm{u}} + x_0 \\ y_{\mathrm{l}} = \gamma_{\mathrm{lu}}y_{\mathrm{u}} - D_{\mathrm{ul}}\frac{2\mu}{\lambda_{\mathrm{u}}+\lambda_{\mathrm{l}}}\sin\beta_{\mathrm{W,u}} = \gamma_{\mathrm{lu}}y_{\mathrm{u}} + y_0 \end{cases} \tag{10}$$

where $\beta_{\mathrm{W,u}}$ is the sideslip angle. Here a linear axial inflow acceleration from the upper to the lower is assumed, as an improvement to the frequently-used skew angle.[1,18,27]

The inflow acceleration of the upper rotor makes the momentum theory for an isolated rotor not applicable for the lower rotor. Therefore, a global flow mass balance past the planes of the two rotors is applied. The approximation of interaction velocity, $v_{i0,\mathrm{lu}}$, can be yielded from

$$(\lambda_0 + v_{i0,\mathrm{ul}})R_{\mathrm{ul}}^2 + v_{i0,\mathrm{u}}^2 R^2 = v_{i0,\mathrm{l}} R^2 + v_{i0,\mathrm{lu}} R_{\mathrm{ul}}^2 + \lambda_0\left(R^2 + R_{\mathrm{lu}}^2 - S_{\mathrm{lu}}/\pi\right) \tag{11}$$

where S_{lu} is the overlapped area.

Finally, the downwash of the upper rotor (right-hand system) on the lower rotor (left-hand system) can be expressed as

$$v_{i\mathrm{lu}}(\bar{r}, \psi_{\mathrm{l}}) = \begin{cases} \delta_{\mathrm{lu}}\left(v_{i0,\mathrm{u}} + v_{is,\mathrm{u}}\bar{y} - v_{ic,\mathrm{u}}\bar{x}\right) \text{ for } \quad \bar{R}_{xy} \leqslant 1 \\ 0 \text{ for } \quad \bar{R}_{xy} > 1 \end{cases} \tag{12}$$

where

$$\begin{cases} \bar{R}_{xy} = \sqrt{\bar{x}^2 + \bar{y}^2} \\ \bar{x} = \frac{-\bar{r}\cos\psi_{\mathrm{l}} - x_0}{\gamma_{\mathrm{lu}}} \\ \bar{y} = \frac{-\bar{r}\sin\psi_{\mathrm{l}} - y_0}{\gamma_{\mathrm{lu}}} \end{cases}$$

The blades of each rotor are assumed to be identical, flapping with the same periodic motion. The generalized coordinates and their derivatives of one blade are obtained from their truncated Fourier series expansions:

$$\beta(\psi) \approx \beta_{\mathrm{app}}(\psi) = \beta_0 + \sum_{j=1}^{N_{\mathrm{h}}}\left(\beta_{jc}\cos(j\psi) + \beta_{js}\sin(j\psi)\right) \tag{13}$$

where β_{app} is the flapping approximation, and N_{h} is the number of harmonics. Then, β_{app} and its derivates are applied to the flapping equation of a blade, where rotor rigidness is modelled with equivalent spring stiffness.[28] The steady flapping motion is solved by applying the azimuthwise Galerkin technique, [29] where the rotor is considered to be in trim when the flap acceleration, $\ddot{\beta}_{\mathrm{app}}$, coincides with $\ddot{\beta}$. Thus, a set of $(1 + 2N_{\mathrm{h}})$ nonlinear algebraic equations for each rotor is obtained. The first harmonic flapping is critical to flight dynamics, and can well predict the blade bending moments in normal flight. [30] Therefore, $N_{\mathrm{h}} = 1$ is applied in this study.

The control input of the coaxial rotor is defined as

$$\begin{cases} \theta_{\mathrm{u}} = (\theta_0 + \Delta\theta_0) - \left(A_{\mathrm{l}} + A'_{\mathrm{l}}\right)\cos(\psi_{\mathrm{u}} + \Gamma) - \left(B_{\mathrm{l}} + B'_{\mathrm{l}}\right)\sin(\psi_{\mathrm{u}} + \Gamma) \\ \theta_{\mathrm{l}} = (\theta_0 - \Delta\theta_0) - \left(A_{\mathrm{l}} - A'_{\mathrm{l}}\right)\cos(\psi_{\mathrm{l}} + \Gamma) - \left(-B_{\mathrm{l}} + B'_{\mathrm{l}}\right)\sin(\psi_{\mathrm{l}} + \Gamma) \end{cases} \tag{14}$$

The overall calculation flow chart of the coaxial rotor aerodynamics is shown in Fig. 3, where inflow dynamics and flapping dynamics of the rotors are considered.

2.2. Modelling of other aerodynamic parts

The modelling method of other aerodynamic components of the coaxial composite helicopter is similar to that of a conventional helicopter. Some key descriptions in the modeling of coaxial composite helicopters are given here. The aerodynamic interferences of the rotors on the horizontal and vertical tails are considered. The local velocity vector of each empennage can be expressed as follows:

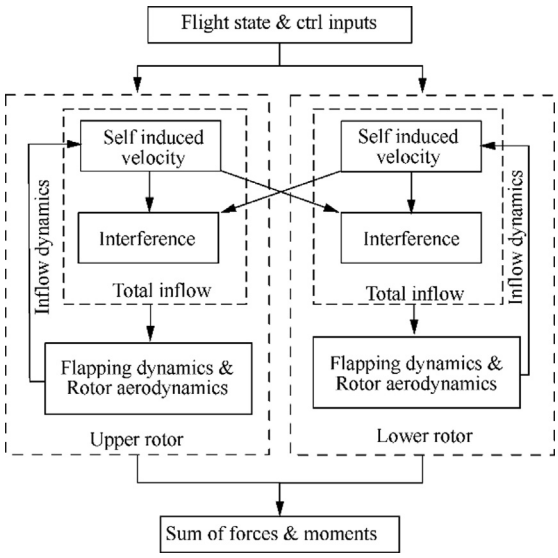

Fig. 3 Structure of coaxial rotor aerodynamics.

$$\begin{cases} \boldsymbol{u}_{\mathrm{H}} = \boldsymbol{u} + \omega \times \boldsymbol{r}_{\mathrm{H}} + \boldsymbol{v}_{i\mathrm{H}} \\ \boldsymbol{u}_{\mathrm{V}} = \boldsymbol{u} + \omega \times \boldsymbol{r}_{\mathrm{V}} + \boldsymbol{v}_{i\mathrm{V}} \end{cases} \tag{15}$$

where $\boldsymbol{v}_{i\mathrm{H}}$ and $\boldsymbol{v}_{i\mathrm{V}}$ are the downwash at the aerodynamic centre of tails. They are assumed as a function of the rotor-induced velocity and the skew wake angle, fitted according to the loading on the stabilizer in the level flight test.[31]

The angles of attack are presented as

$$\begin{cases} \alpha_{\mathrm{H}} = \arctan\frac{w_{\mathrm{H}}}{u_{\mathrm{H}}} + \alpha_{\mathrm{H0}} + k_{\mathrm{e}}\delta_{\mathrm{e}} \\ \alpha_{\mathrm{V}} = \arctan\frac{v_{\mathrm{V}}}{u_{\mathrm{V}}} + \alpha_{\mathrm{V0}} + k_{\mathrm{r}}\delta_{\mathrm{r}} \end{cases} \tag{16}$$

where $\alpha_{\mathrm{H0}}, \alpha_{\mathrm{V0}}$ are the installation incidences of the horizontal and vertical tails, respectively;$k_{\mathrm{e}}, k_{\mathrm{r}}$ are the efficiency factors of the elevator and rudder, respectively, and are related to Mach number and deflection angles,$\delta_{\mathrm{e}}, \delta_{\mathrm{r}}$. According to the local angles of attack, the lift and drag coefficients $C_{DH}, C_{LH}, C_{DV}, C_{LV}$ can be obtained from a 2-D airfoil aerodynamics look-up table with the velocity vectors $\boldsymbol{u}_{\mathrm{H}}$ and $\boldsymbol{u}_{\mathrm{V}}$, respectively.

The aerodynamic interference of the rotors on the fuselage is fitted as a function of the rotor-induced velocity and the skew wake angle, according to the wind test data in Ref. 32 and discussion from Kim et al.[33] Then the local velocity vector of the fuselage aerodynamic center can be expressed as follows:

$$\boldsymbol{u}_{\mathrm{F}} = \boldsymbol{u} + \omega \times \boldsymbol{r}_{\mathrm{F}} + \boldsymbol{v}_{i\mathrm{F}} \tag{17}$$

where $\boldsymbol{v}_{i\mathrm{F}}$ is the rotor downwash at the fuselage. Thus, the attack and sideslip angles of the fuselage can be determined. The fuselage aerodynamic loads are calculated using the scaled aerodynamic load coefficients from the wind tunnel test. [25,32] In the hover state, the downwash on the fuselage causes a large angle of attack. Thus, a dataset of force and moment coefficients from Ref. 28 is applied to determine the fuselage aerodynamics.

A propeller is applied according to the development of the coaxial compound helicopter in recent years. Parameters of the propeller are the same as those given in Ref. 2. The propeller model is similar to the rotor model, but does not consider

flapping motion and inflow interference. A dynamic uniform inflow, as expressed by Eq. (18), is applied

$$\dot{v}_{\mathrm{ip}} = \frac{3\pi}{4}\left(\frac{C_{T\mathrm{p}}}{2} - v_{\mathrm{ip}}\sqrt{\mu_{\mathrm{p}}^2 + \left(\lambda_{\mathrm{p}} + v_{\mathrm{ip}}\right)^2}\right) \tag{18}$$

where variables are defined in the propeller axis system.

2.3. Trim strategy

The propeller pitch control makes the unknown trim variable exceed the number of trim equations by one. Therefore, an additional constraint is added. That is, the propeller is trimmed for a targeted level-flight pitch attitude. According to the flight test of X2TD,[8] a minor upflow from nose-up can increase rotor aerodynamic efficiency. Therefore, a constant pitch attitude (2°) is assumed.

The coaxial rotor speed is slowed to delay the compressibility effect at the advancing blade tip in high-speed flight. Therefore, the rotor speed is set as[34]

$$\Omega = \begin{cases} \Omega_0 & V < 70\ \mathrm{m/s} \\ \Omega_0\left(1 - \frac{V-30}{300}\right) & V \geqslant 70\ \mathrm{m/s} \end{cases} \tag{19}$$

As demonstrated in Ref. 2, the strong coupling between the differential collective control and lift offset at high speeds can significantly degrade flight performance. In addition, the control power of the differential control $\delta_{\Delta\theta_0}$ reduces quickly as airspeed increases, while that of the rudder increases.[35] Therefore, the pedal control, δ_{ped}, is designed as

$$\begin{cases} \delta_{\Delta\theta_0} = \varepsilon\delta_{\mathrm{ped}} \\ \delta_{\mathrm{r}} = (1-\varepsilon)\delta_{\mathrm{ped}} \end{cases} \tag{20}$$

where ε represents the linear washout of collective differential control between 20–40 m/s.

Finally, a flight dynamics model of the coaxial compound helicopter is established. It contains 22 Degrees of Freedom (DOFs), including nine DOFs of the fuselage rigid motions, six DOFs of the induced velocities of the coaxial rotor, six DOFs of flapping motions of the coaxial rotors, and one DOF of the propeller induced velocity. The flight dynamics model for the aircraft is expressed in the form of

$$\dot{\boldsymbol{X}} = \mathrm{F}(\boldsymbol{X}, \boldsymbol{U}, t) \tag{21}$$

where

$$\begin{cases} \boldsymbol{X} = [\,\boldsymbol{x}_{\mathrm{F}}, \boldsymbol{x}_{\beta}, \boldsymbol{x}_{v_i}\,]^{\mathrm{T}} \\ \boldsymbol{U} = [\boldsymbol{u}_1, \boldsymbol{u}_2] \end{cases}$$

where $\boldsymbol{X}$ is the state vector, containing the aircraft state vector $\boldsymbol{x}_{\mathrm{F}}$, coaxial rotors flapping state vector $\boldsymbol{x}_{\beta}$, and inflow state vector $\boldsymbol{x}_{v_i}$; $\boldsymbol{U}$ is the control variable vector, with $\boldsymbol{u}_1$ referring to the general control variables, including $\theta_0, A_1, B_1, \Delta\theta_0$ and θ_{p}, and $\boldsymbol{u}_2$ referring to two unique controls of the compound coaxial helicopter, A_1', B_1'.

3. Steady flight validation

The coaxial compound helicopter is modelled according to the parameters of XH-59A. The data of XH-59A are available from the public technical report,[6] but its airfoil data are unavailable yet. Therefore, in our study, the airfoils that match the thickness distribution of the actual foils are used:[25] NACA 0026 is used for $\bar{r} < 0.4$, NACA 63–218 is used for $0.4 \leqslant \bar{r} \leqslant 0.65$, and NACA 23012 is used for $\bar{r} > 0.65$.

It is important to verify the accuracy of the interference between the rigid coaxial rotors. Here, the flight test data of the pure coaxial configuration[6] are used, and are compared with the trim results. In the flight, the rotor control phase angle Γ is scheduled as

$$\Gamma = \begin{cases} 40^\circ & V < 40\ \mathrm{m/s} \\ 50^\circ & 40\ \mathrm{m/s} \leqslant V \leqslant 50\ \mathrm{m/s} \\ 60^\circ & V > 50\ \mathrm{m/s} \end{cases} \tag{22}$$

to alter the Lift Offset (LOS), so as to improve rotor aerodynamic performance.

An accurate flow model is vital for the behavior prediction of the coaxial rotor. The inflow in this paper consists of self-induced velocity and interference. The former is presented as harmonic inflow, leading to the latter in a similar harmonic form. In contrast, the inflow distributions obtained from vortex-wake-based methods[14,16,17] are usually highly non-uniform. In order to quantify the non-uniform distribution for model validation, the rotor inflow is fitted into the form of

$$v_i(\bar{r}, \psi) = v_{i0} + \bar{r}\, v_{is}\sin\psi + \bar{r}\, v_{ic}\cos\psi \tag{23}$$

by applying the least squares method.

The fitting results from calculation and Ref. 14 are presented in Fig. 4. The components of the inflow on each rotor are also presented. The interference on the upper rotor is smaller than the self-induced inflow. In contrast, the lower rotor is subjected to strong harmonic downwash from the upper rotor. The general inflow distribution shows a similar trend regarding velocity, indicating the accuracy of the proposed BEMT model.

Fig. 5 shows the trim validation of the coaxial rigid-rotor helicopter. The results with interference are in good agreement with the flight test. It indicates the accuracy of the proposed aircraft dynamics model, which could be used to simulate the flight dynamics of the rotorcraft. Results without aerodynamic interference are also provided for comparison. The mutual interference influences the trim characteristics, especially in hover and low-speed flight ($\mu = 0 \rightarrow 0.2$). It could be found that the interference has significant influence on the flight dynamics of the aircraft. Within this speed range, the additional downwash onto each rotor reduces the thrust of the coaxial rotor at a given collective pitch. Meanwhile, the longitudinal stick is pushed forward more.

In a conventional helicopter, the increase of airspeed causes the rotor to tilt backward. In addition, there is high downwash onto the horizontal tail. The two factors generate nose-up moments. The coaxial compound helicopter is equipped with a large tail for incidence stability, which generates more pitching moments. Moreover, the aft side of the lower rotor is affected by the upper rotor's wake, causing extra moments. As a result, an additional longitudinal cyclic control is required, leading to a negative longitudinal gradient through the range of $\mu = 0.1 - 0.2$, as shown in Fig. 5.

The pitch attitude is below -10° at high speed to balance the airframe drag due to low propulsion from rigid rotors.

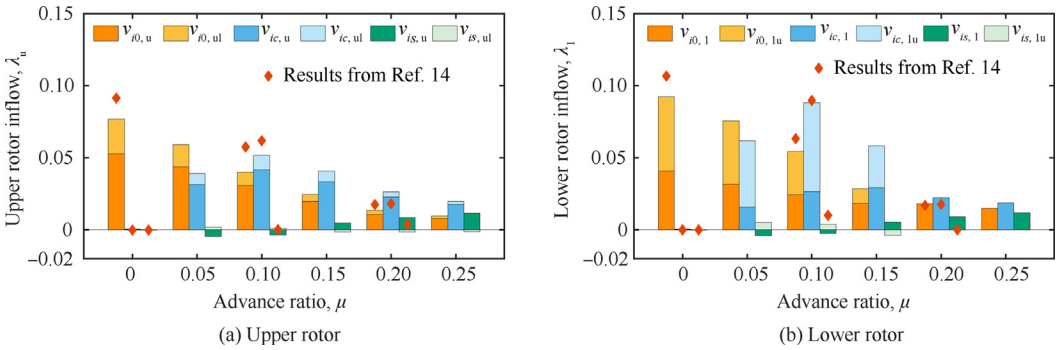

Fig. 4 Validation of inflow distribution of coaxial rotors.

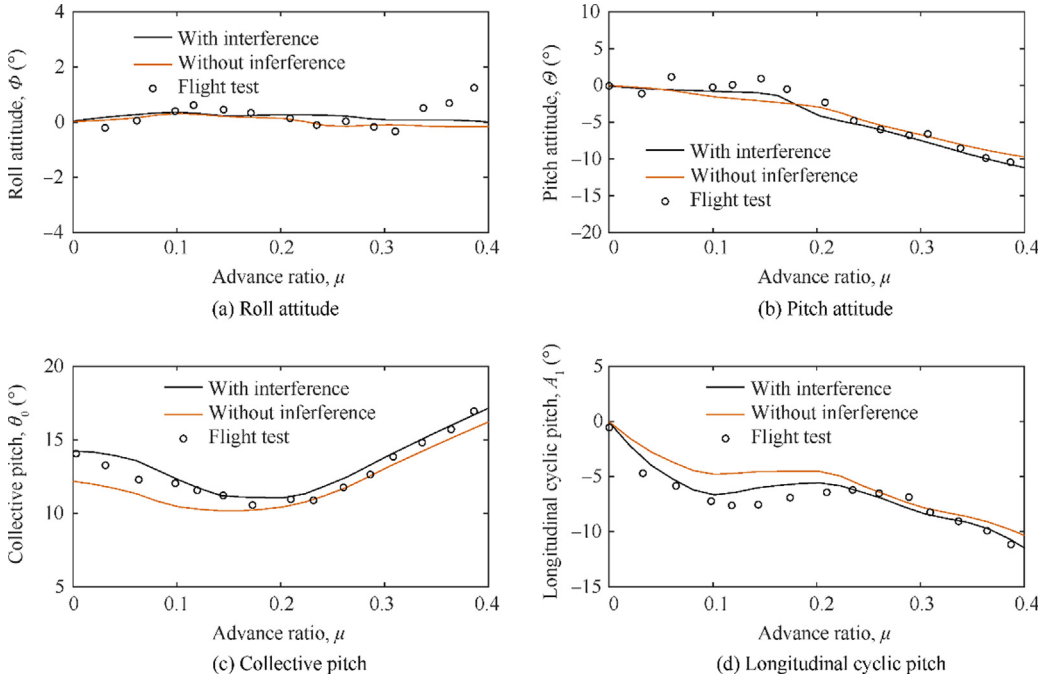

Fig. 5 Validation of trim result and related influence by interference.

Nevertheless, the pitch attitude is level until the advance ratio of 0.15 due to sufficient propulsion from the high longitudinal stick input.[31]

As the speed increases over 40 m/s ($\mu = 0.2$), the aerodynamic interference decreases. Thus, the results with and without interaction are of similar patterns. The subtle higher collective and longitudinal inputs in the interference case are caused by the high inflow from the high nose-down, which retains minor interference.

4. Trim analysis

This section investigates the influence of DLCP on trim characteristics, and the results indicate that a negative A_1' is recommended. Therefore, various DLCPs are presented in the descending order to illustrate the variation trend.

4.1. Attitude and stick movements

Fig. 6 shows the trim results of attitude and control sticks, with varying DLCP. The case without rotor interference is also provided for comparison. The high-speed region shows subtle lateral and heading changes and hardly any longitudinal variation. By contrast, within the speed region with interference ($\mu < 0.2$), the DLCP significantly influences the flight dynamics of the coaxial compound helicopter. It indicates the DLCP affects the interaction between the coaxial rotors.

The influence of DLCP, ($-A_1'$), is illustrated in Fig. 7. The coaxial rotor system provides nose-down moments to balance the coaxial compound helicopter. If $A_1' = 0$, the lower rotor has a slightly lower nose-down moment due to the interaction. A negative DLCP increases the nose-down moment on the upper rotor, but decreases that on the lower rotor. The signif-

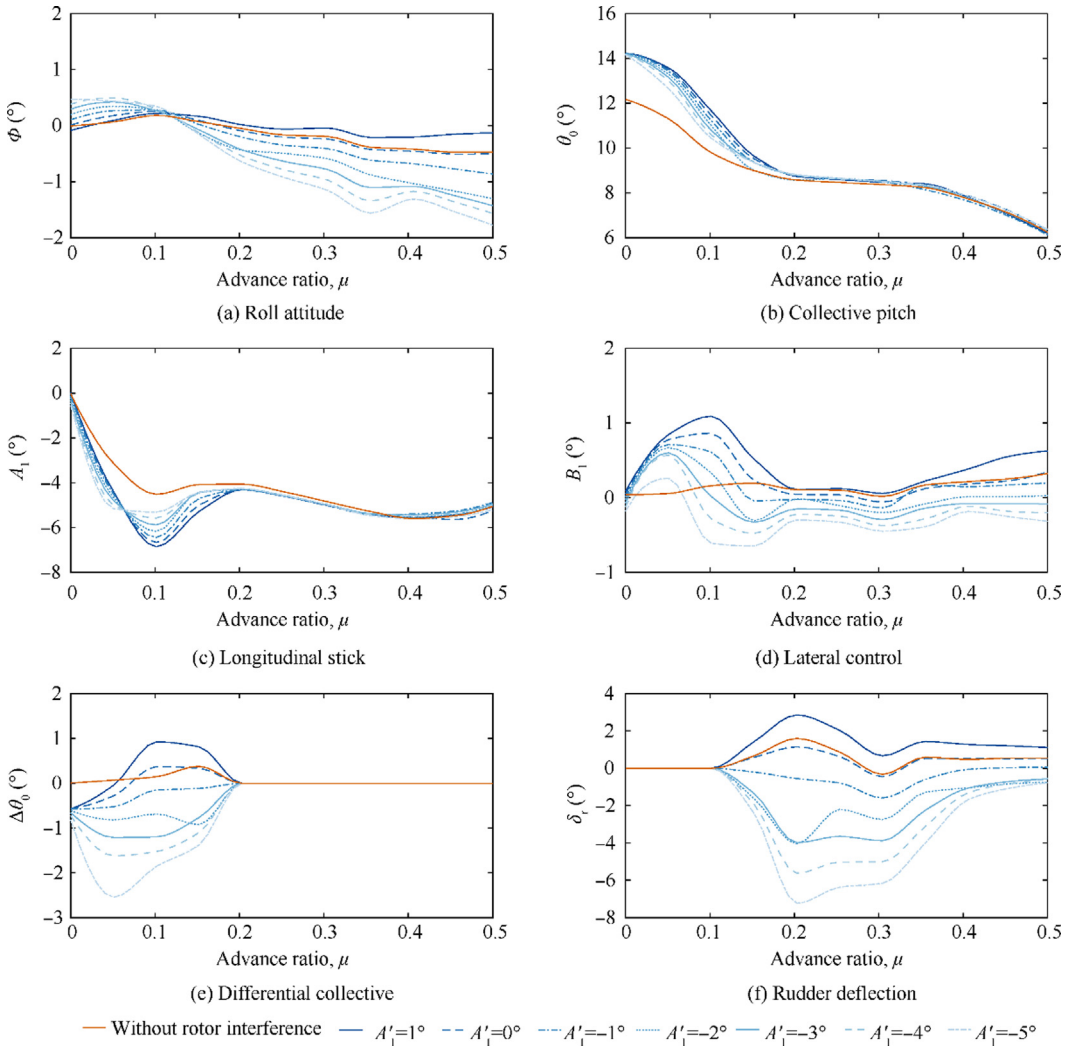

Fig. 6 Variation of trim state of attitude and stick movements.

icant variation of aerodynamic force changes the harmonic inflow and flapping motion. Conversely, the induced velocity changes aerodynamic loads. As a result, the control inputs and airframe attitude are changed for trim balance.

In the hover state, there is hardly any variation with A_1' due to symmetric rotors, except for the subtle roll attitude. A right roll is needed to balance the extra profile drag from the upper rotor (less than 50 N), whose rotor aerodynamics is degraded by the negative A_1'.

As speed increases to around 10 m/s, stick displacements change with varying A_1'. The DLCP changes the pitching moments on the coaxial rotor and the harmonic inflow. Conversely, the induced velocity changes the aerodynamic loads. Therefore, the inflow variation is the critical factor of the DLCP. Fig. 8 presents the contour figures of the induced velocities on the upper and lower rotors, with $A_1' = 0$. The flow distribution indicates that the lower rotor operates in the full wake contraction of the upper rotor. At the rear edge of the rotor disk (azimuth 0°), the total downwash is around 30 m/s. Meanwhile, the induced velocity does not vary along the $90^\circ - 270^\circ$ azimuth axis because of the anti-symmetry of the coaxial rotor and similar aerodynamic loads at the rotor advancing and retreating sides.

The inflow of coaxial rotors is in a near-linear pattern along $0^\circ - 180^\circ$ azimuth axis. The fitting method shown in Eq. (23) is applied to quantify the influence of DLCP on inflow distribution. Variation of the fitted inflow with A_1' is given in Fig. 9, and the results without interference are also included for comparison. Only the uniform and cosine harmonic terms are provided, and the sine harmonic is omitted considering its minor amplitude.

The collective and differential collective pitch variations are related to the uniform inflow. Negative DLCP results in more harmonic airflow on the upper rotor, aggravating the non-uniformity of the inflow. The degraded aerodynamics leads to a higher torque moment. Hence, the collective pitch of the lower rotor is increased for torque balance, i.e., a negative differential collective pitch ($\Delta\theta_0$) is required. Consequently, the lift is changed. In order to illustrate the lift variation clearly, the classical momentum theory is used as the analytical model.

$$\begin{cases} C_{T\mathrm{u}} = v_{i0,\mathrm{u}}\sqrt{\mu^2 + (\lambda_0 + v_{i0,\mathrm{u}} + v_{i0,\mathrm{ul}})^2} \\ C_{T\mathrm{l}} = v_{i0,\mathrm{l}}\sqrt{\mu^2 + (\lambda_0 + v_{i0,\mathrm{l}} + v_{i0,\mathrm{lu}})^2} \end{cases} \tag{24}$$

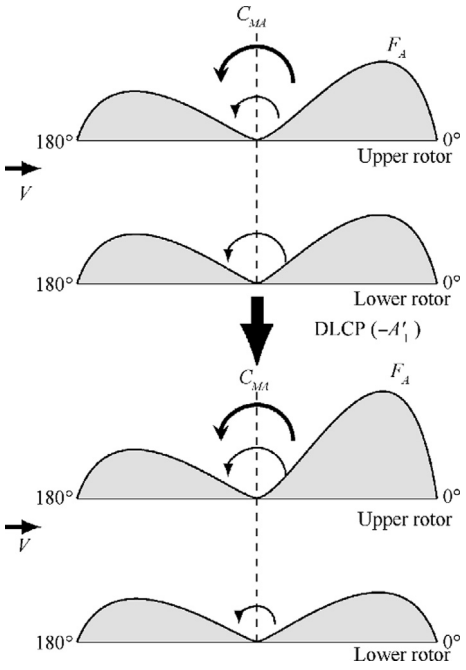

Fig. 7 DLCP control.

A reduced collective pitch on the upper rotor results in less induced velocity ($v_{i0,u}$), reducing interference to the lower rotor ($v_{i0,lu}$). As a result, the lower rotor generates more thrust, thus less collective pitch is required.

The longitudinal stick is pushed forward with DLCP. In the ideal case with no interference, the DLCP merely changes the inner pitching moments in antisymmetric coaxial rotors, and the total pitching moment is not influenced. However, the lower rotor is subjected to higher downwash from the upper rotor, as shown in Fig. 9. Consequently, the nose-up moment is increased, leading to more longitudinal stick displacements.

Variation of the lateral stick is relevant to the harmonic inflow as well, due to complex coupling between the flapping motion and aerodynamic forces. Generally speaking, there is a phase difference between the aerodynamic moment generated by the airflow and the hub moment acting on the body. The phase difference is also known as the flapping response lag ϕ_f, resulting from the harmonic motion. The phase lag between the exciting force and response can be approximately expressed as[14]

$$\cos\phi_f = \frac{\bar{\omega}_n^2 - 1}{\sqrt{\left(\bar{\omega}_n^2 - 1\right)^2 + 4\zeta^2\bar{\omega}_n^2}} \tag{25}$$

where ζ is the aerodynamic damping ratio, approximately

$$\zeta = \frac{\gamma_b}{16\bar{\omega}_n}$$

for a blade without blade root lift loss.

The flapping response lag of the conventional helicopter is about 90°, with the first-order flapping frequency approximating 1.0/rev. Therefore, aerodynamic pitching moments typically generate rolling moments on the body. By contrast, the stiffness of the coaxial rigid rotor is much higher, with ω_n being around 1.4–1.5/rev. Thus, the phase lag, ϕ_f, is approximately 30°-40° according to Eq. (25). As a result, the downwash interference, the key factor altered by DLCP, causes both pitching and rolling hub moments. The phase angle results in left-rolling hub moments from the lower rotor due to the interference. Thus, the lateral stick is pushed right for balance.

In order to illustrate the variation of lateral stick with DLCP, the aerodynamic pitching moment is analysed. As A_1' varies from 1° to −5°, distribution of the lower rotor inflow does not vary significantly, as shown in Fig. 9. However, the aerodynamic moment is changed. The relationship between the cosine harmonic inflow and the aerodynamic moment of the lower rotor can be presented as

$$\frac{15\pi}{64v_T}\tan\frac{\chi_l}{2}C_{Tl} - \frac{4\cos\chi_l}{v_M(1+\cos\chi_l)}C_{MAl} = v_{ic,l} \tag{26}$$

where

$$\begin{cases} v_T = \sqrt{\mu^2 + \lambda_l^2} \\ v_M = \frac{\mu^2 + \lambda_l\left(\lambda_l + v_{i0,1}\right)}{v_T} \end{cases}$$

according to the Pitt-Peters dynamic inflow method.[23]

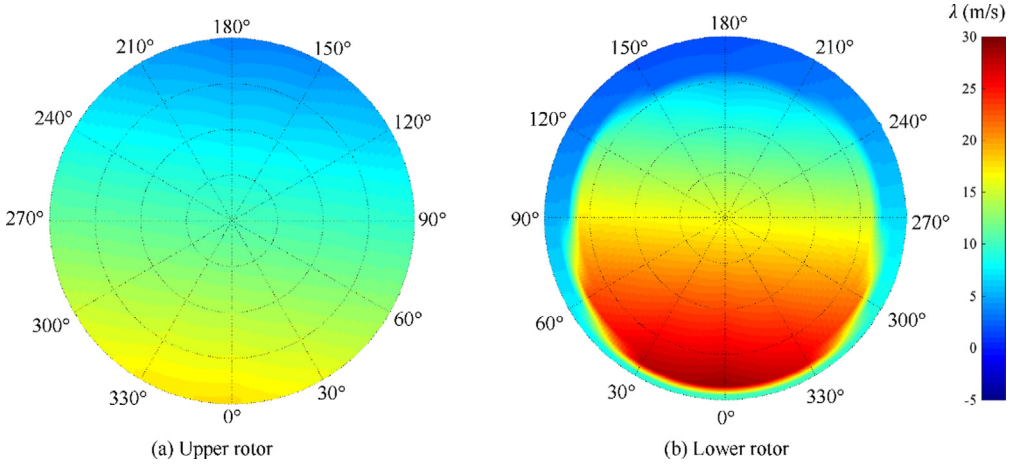

Fig. 8 Inflow distribution when $\mu = 0.05$ (lower rotor on the right, $A_1' = 0$).

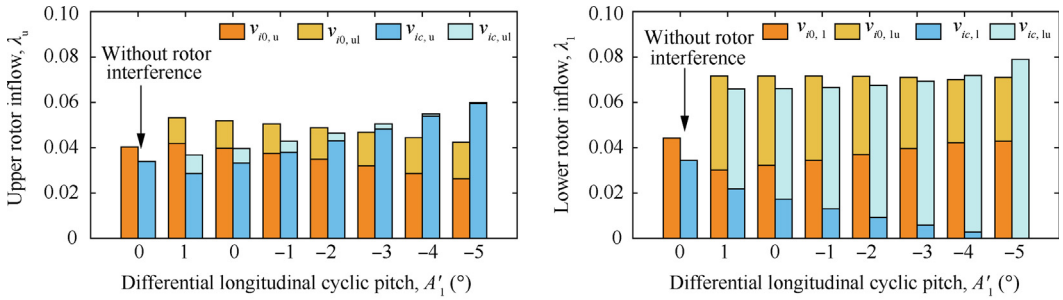

Fig. 9 Variation of inflow with DLCP control when $\mu = 0.05$.

Therefore, the aerodynamic pitching moment is alleviated due to the reduced self-induced airflow, in line with the influence of DLCP. As a result, there is fewer hub left-rolling moments, leading to less lateral stick.

As the advance ratio reaches 0.1, the upper rotor wake primarily affects the aft side (azimuth 0°) of the lower rotor, and the interference area is partially outside the rotor disk. Fig. 10 presents the contour figures of the induced velocities on coaxial rotors, with $A_1' = 0$. The lower rotor is subjected to a highly non-uniform inflow due to the interference from the upper rotor. There is very large downwash (up to around 30 m/s) within the range of $-60^\circ - 60^\circ$ azimuths, indicating the rearward translation of the interference. By contrast, the fore region has much lower airflow, ranging between − 5 m/s and 5 m/s due to the upflow from the upper rotor. The highly non-uniform distribution results in high aerodynamic pitching moments, leading to large longitudinal and lateral cyclic pitches for trim balance, as shown in Fig. 6. The influence of DLCP on the fitted inflow is given in Fig. 11.

The collective and differential collective variations are similar to those in the case of $\mu = 0.05$ for the same reason. Moreover, the amplitude is higher due to improved lower rotor efficiency. The reasons are as follows. Less harmonic airflow is generated as partial downwash from the upper rotor outside the lower-rotor disk. Meanwhile, the reduced uniform flow, $v_{i0,u}$ further leads to backward translation of the interference area (Eq. (10)). Consequently, the lower rotor is subjected to lower extra inflow, as shown in Fig. 11, resulting in improved rotor efficiency.

The lateral stick displacement is reduced as the DLCP decreases. One reason is the same as that when $\mu = 0.1$. The other factor is relevant to the improved lower rotor aerodynamics. The advancing blade generates more rolling moments, causing left lateral cyclic pitch ($-B_1$).

Different from the case of $\mu = 0.05$, the longitudinal control decreases with A_1' for two reasons. The first and most important is the inflow variation that changes the hub moment. The upper rotor generates more nose-down moments due to the reduced uniform inflow. In addition, the lower rotor needs less longitudinal cyclic pitch owing to the reduced interaction. The other factor is the lowered rotor collective pitch. It alleviates the rearward flapping due to the forward free-flow, leading to fewer pitching moments. As a result, the negative longitudinal gradient from $\mu = 0.1$ to 0.2 is alleviated.

When the advance ratio increases to around 0.2 or higher, there is no significant interference between coaxial rigid rotors. The DLCP does not change longitudinal states, because A_1' results in pitching moments of the same value with opposite direction, without changing total moments. However, it slightly affects the lateral and heading control. As illustrated in Fig. 7, a negative A_1' generates more nose-down moment on the upper rotor. As a result, the aerodynamic condition of the upper rotor is degraded, while that of the lower rotor is improved. This leads to more thrust produced by the lower rotor and less by the upper one. Thus, more rolling moments and forces are produced from the advancing blade of the lower rotor, leading to a left roll attitude and left pushed stick for balance. Meanwhile, the rudder is adjusted for torque balance. Another reason is due to the flapping characteristics of the rigid rotor. During flight tests of XH-59A,[6] the 60° control phase, ($\Gamma > \phi_f$), results in right rolling moment with $-A_1'$. In the case studied in this paper, the flapping phase lag ϕ_f becomes slightly smaller than the control phase Γ (40°) as forward flight speed increases.[2] Consequently, a minor left stick displacement is needed.

4.2. Performance evaluation

The influence of DLCP on the performance of the coaxial compound helicopter is studied in this section. Fig. 12 shows the power consumption of the rotor system and propeller. There are significant power variations when the advance ratio is between 0–0.2, where the interference is changed. Table 1 shows the average power compared with the baseline ($A_1' = 0^\circ$) within the speed range.

Fig. 12(a) and Table 1 show that the rotor power is alleviated by around 4.7% when $A_1' = -3^\circ$. A higher negative DLCP, despite the reduced interference and the low collective pitch, results in higher power consumption. This is caused by unbalanced thrust allocation between coaxial rotors. The lower rotor has much higher thrust according to the negative differential collective pitch. Consequently, the induced power is increased, especially when $A_1' = -5^\circ$ and $\mu = 0.05$. This means that unbalanced lift distribution between coaxial rotors can degrade power efficiency.

The propeller power required is increased with varying A_1' for different reasons. The reduced longitudinal sticks in the negative cases, A_1', generate fewer forward forces. Thus, more propeller propulsion is needed, and the power required increases tremendously with A_1'. As a result, the best performance improvement is achieved when $A_1' = -3^\circ$. On the other

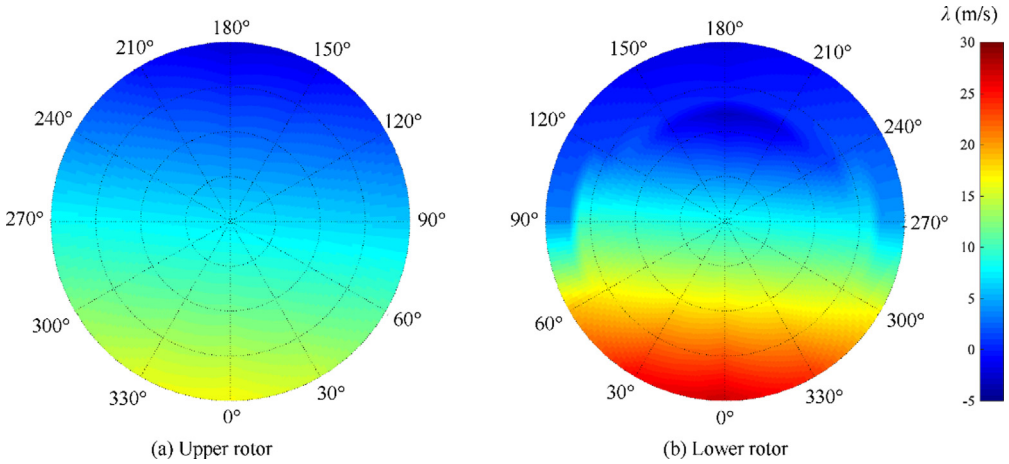

Fig. 10 Inflow distribution when $\mu = 0.1$ (lower rotor on the right, $A_1' = 0$).

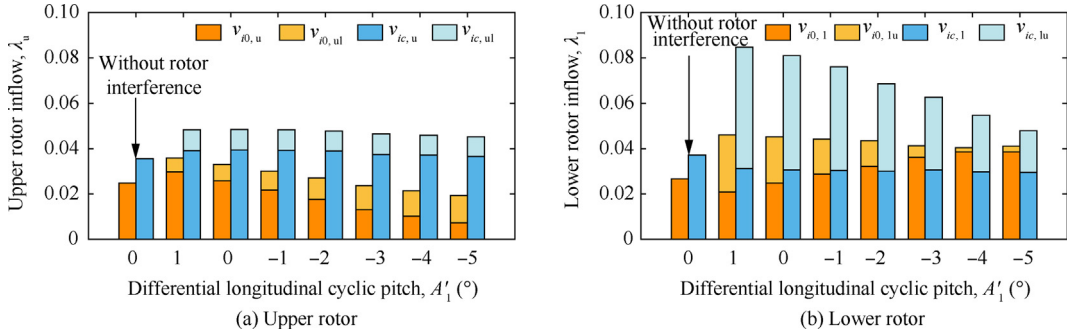

Fig. 11 Variation of inflow with DLCP control when $\mu = 0.1$.

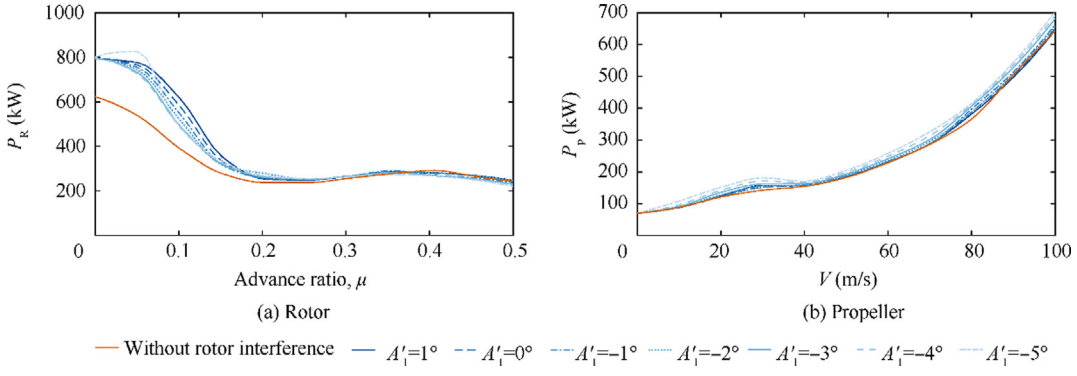

Fig. 12 Variation of average power with DLCP.

hand, the power is also increased despite the high stick input when $A_1' = 1^\circ$. It is because of a higher profile drag from the degraded rotor aerodynamic performance. Finally, the highest total power reduction is achieved when $A_1' = -3^\circ$.

4.3. Tip clearance

Maintaining safe tip clearance is a crucial design target in developing and testing counter-rotating coaxial rotors. The tip clearance can be calculated according to the flapping motion of the two rotors:

$$D_{\min} = D_{\mathrm{lu}} + R(\beta_{0\mathrm{u}} - \beta_{0\mathrm{l}}) - R \times \sqrt{(\beta_{s\mathrm{u}} + \beta_{s\mathrm{l}})^2 + (\beta_{c\mathrm{u}} - \beta_{c\mathrm{l}})^2} \quad (27)$$

As airspeed increases, more aerodynamic rolling moment is generated on the advancing blade. In a conventional helicopter, the roll moment generates a high pitch hub moment. However, flapping lag also results in lateral flapping on the

Table 1 Average power consumption increments due to DLCP when $\mu \in [0, 0.2]$.

$A_1'(^\circ)$	Average power consumption increment(%)		
	Total	Rotor	Propeller
1	2.16	2.31	1.45
0	0	0	0
−1	−1.82	−2.24	0.14
−2	2.06	−2.86	1.63
−3	−2.90	−4.68	5.35
−4	−2.14	−4.66	9.51
−5	2.33	−0.51	15.41

advancing side (β_{su}, β_{sl}) in the hingeless rotor, leading to reduced tip clearance, as shown in Fig. 1. The trend is in accordance with the results in Refs. 3,9. Finally, the decreased tip clearance is well above the safe margin of 0.25 m.[8]

According to Fig. 13, a negative A_1' reduces the tip clearance throughout the speed range due to three factors. The most direct reason is that A_1' changes the longitudinal flapping motion. This leads to the nose-down flapping of the upper rotor (reduced β_{cu}) and nose-up flapping of the lower rotor (increased β_{cl}). Consequently, the tip clearance is degraded, which is in line with the results obtained from the flight test of XH-59A.[6] Meanwhile, more tip clearance is reduced at low speeds because of higher lift from the lower rotor. Finally, it reduces most when $\mu \approx 0.05$, where the increased downwash causes more nose-up flapping of the lower rotor.

In summary, a suitable DLCP control can alleviate the low-speed interference and improve rotor efficiency. As the advance ratio reaches above 0.2 with subtle interference, A_1' does not benefit the rotorcraft's flight performance. Therefore, it is recommended to introduce DLCP for low-speed flights.

5. Dynamic stability analysis

According to the trim results, the DLCP influences the rotor efficiency and flight dynamics of the rotorcraft. The altered mutual interference changes the aerodynamic loads of the rotorcraft. Meanwhile, the DLCP changes the flapping motion and further affects the stability derivatives of the rotors. Therefore, the dynamic stability of the aircraft with various A_1' is investigated. Two representative speeds, $\mu = 0.05$ and 0.1, are discussed. The longitudinal and lateral dynamic stability are given in Figs. 14 and 15, respectively.

According to Fig. 14, a negative A_1' decreases the pitch subsidence, which is primarily determined by pitch damping M_q.M_q is related to two moments: one is the aerodynamic moment from the angular motion, and the other is from the gyroscopic flapping moment. In an articulated rotor with phase lag $\phi_f = 90^\circ$, the pitch damping and coupled roll derivative are given by[36]

$$\begin{cases} \frac{\partial \beta_c}{\partial q} = \frac{1}{\sqrt{\left(\bar{\omega}_n^{-2}-1\right)^2 + 4\zeta^2\bar{\omega}_n^{-2}}} \cdot \frac{2}{\Omega} = \frac{16}{\gamma_b \Omega} \\ \frac{\partial \beta_s}{\partial q} = -\frac{1}{\sqrt{\left(\bar{\omega}_n^{-2}-1\right)^2 + 4\zeta^2\bar{\omega}_n^{-2}}} \cdot \frac{\gamma_b}{8\Omega} = -\frac{1}{\Omega} \end{cases} \tag{28}$$

where $\partial\beta_c/\partial q$ is relevant to the derivative from the gyroscopic moment, and $\partial\beta_s/\partial q$ refers to damping from aerodynamic loads. Adapted to the counter-rotating coaxial rotor system, the damping is

$$\frac{\partial \beta_{cl}}{\partial q} = \frac{\partial \beta_{cu}}{\partial q} = \frac{2\sin\phi_f + (\gamma_b/8)\cos\phi_f}{\Omega\sqrt{\left(\bar{\omega}_n^{-2}-1\right)^2 + 4\zeta^2\bar{\omega}_n^{-2}}} \tag{29}$$

where the ideal anti-symmetry flapping motion of coaxial rotors is assumed.

In an articulated coaxial rotor system, the pitch damping only depends upon gyroscopic moment, unaffected by aerodynamic loads. In the rigid rotor, the influence of aerodynamic damping increases due to the phase lag of around 30° to 40°. M_q decreases as A_1' varies from 1° to -5°. To explain this, the pitch rate, q, is regarded as the equivalent harmonic inflow (v_{ic}) in terms of the aerodynamic effect. The pitch rate influences the aerodynamic moment. According to the Pitt-Peters dynamic inflow (Eq. (3)), the harmonic airflow alleviates the influence of pitch rate. In other words, the damping effect is degraded, especially when the self-induced term has a high ratio in total airflow. As a result, the coaxial rigid rotor with a large negative A_1' has less damping due to its lower additional inflow.

The heave subsidence is related to the damping derivative Z_w.[28] At low speeds, upflow perturbation influences the aerodynamic forces and the induced inflow. According to the momentum theory, the induced airflow tends to offset the effect of free airflow. What's worse, the interaction from the upper rotor degrades lower rotor lift. Therefore, $|Z_w|$ slightly increases in the case of a negative A_1', when interference is lower.

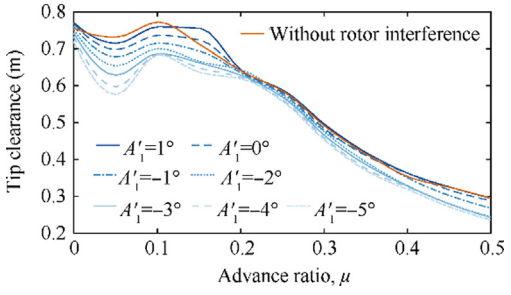

Fig. 13 Tip clearance variation.

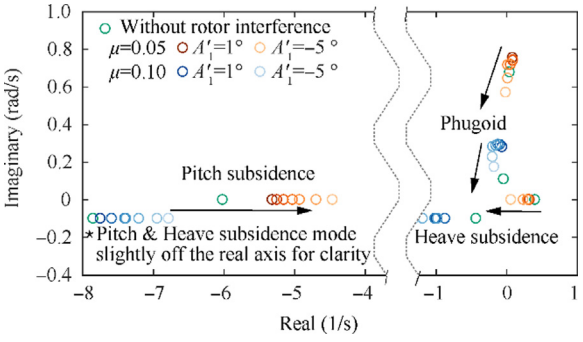

Fig. 14 Longitudinal stability when $\mu = 0.05, 0.10$.

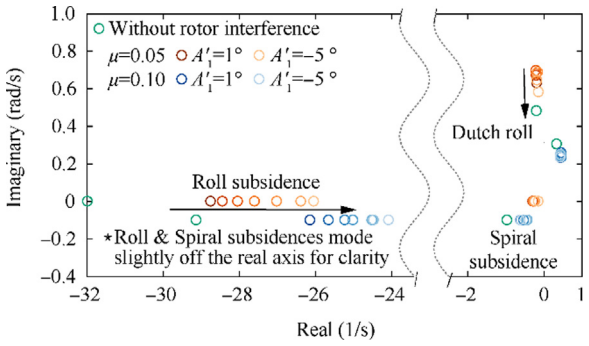

Fig. 15 Lateral stability when μ = 0.05, 0.10.

According to Ref. 28, the powerful M_u and M_w are the main factors relevant to phugoid stability in the rigid hingeless rotor. The incidence instability, M_w, is alleviated with DLCP. The explanation is as follows. A vertical upflow perturbation results in higher induced velocity on the upper rotor. Then higher interference on the aft side of the lower rotor generates extra pitching moments. As a result, the upflow extravagates the incidence instability. In other words, the negative A_1 reduces M_w due to the alleviated interaction. In a conventional helicopter, the speed stability, M_u, is caused by the aerodynamic load increment of the advancing side. By contrast, the interference in coaxial rotors complicate the response to speed perturbation. An increase of speed results in rearward translation of the interference, especially in high DLCP cases with low inflow. Therefore, the speed stability, M_u, is slightly reduced. Combined with the alleviated incidence instability, the stability of phugoid mode is slightly improved.

The roll subsidence and dutch roll, shown in Fig. 15, are similar to the trend of pitch subsidence and phugoid mode, respectively, because of the strong lateral and longitudinal coupling. The amplitude of roll subsidence is much larger due to the aircraft's low roll inertia, I_{xx}. In a conventional helicopter, the spiral and dutch roll modes typically involve excursions in the lateral velocity, along with roll and yaw attitude motion.[28] However, in the coaxial compound helicopter, the vertical fin is of low dynamic pressure and does not significantly influence the yaw motion. In addition, it is hardly affected by the inflow variation, leading to unaffected spiral subsidence. Hence, there is hardly any difference in the spiral subsidence (stability is determined by the yaw damping N_r).

6. Controllability analysis

The controllability of the coaxial compound helicopter is affected by A_1' . Firstly, the induced velocity tends to offset the aerodynamic perturbation. Thus, different airflow changes the force/moment derivate regarding control. In addition, the DLCP changes the flapping motion of each rotor, leading to different responses to stick inputs. Therefore, the controllability at various DLCPs is investigated, and the results are given in Fig. 16.

The on-axis control derivatives of the collective and differential collective are given in Fig. 16(a). Generally speaking, a positive collective pitch increases rotor thrust, and results in higher induced inflow. The airflow offsets the force increment conversely. According to the momentum theory (Eq. (24)), additional downwash alleviates the variation of induced velocity, consequently benefiting the control power. Therefore, the collective pitch derivate, Z_{θ_0}, reduces with DLCP due to the alleviated downwash.

By contrast, the differential collective derivate, $N_{\Delta\theta_0}$, shows a complex trend with DLCP. The heading moment is analysed based on the power required. DLCP mainly influences the induced power, multiplication of the thrust and induced inflow. The induced power variation can be evaluated by

$$\delta(C_T\lambda) = \delta C_T\lambda + C_T\delta\lambda \tag{30}$$

A negative differential collective pitch increases the lift on the lower rotor. According to the analysis of Z_{θ_0}, the thrust increment decreases with DLCP, while the induced velocity variation increases with DLCP. Finally, the induced power first decreases and then increases.

The longitudinal control power shows different trends at different speeds. When the advance ratio is 0.05, a positive longitudinal cyclic pitch, A_1', increases the harmonic inflow on the upper rotor. Then, the downwash to the lower rotor offsets the effect of the cyclic pitch. Therefore, a negative A_1' has higher

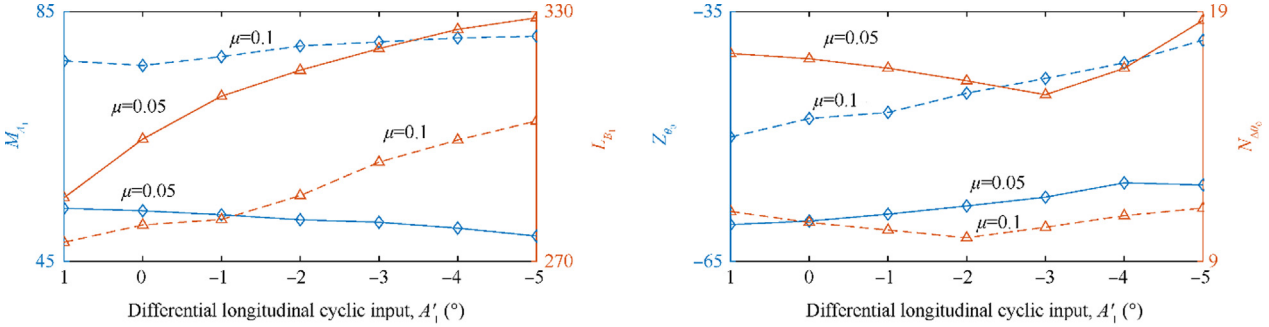

(a) Collective and differential collective control derivates

(b) Longitudinal and lateral cyclic control derivates

Fig. 16 On-axis controllability when $\mu = 0.05, 0.1$.

harmonic inflow, amplifying the reduction of M_{A_1}. On the other hand, in the case of $A_1' = -5^\circ$ and $\mu = 0.1$, the longitudinal derivative is higher due to the alleviated harmonic inflow.

Different from the longitudinal derivate, the lateral control power shows an increasing trend with the DLCP at the two speeds. This is because A_1' mainly influences the cosine harmonic inflow, while the sine harmonics is around zero. Thus, the lateral derivative is hardly affected by the harmonic airflow. When DLCP is lowered to -5°, the lower rotor operates under an improved aerodynamic condition, increasing the lateral control derivate.

7. Conclusions

This paper investigated the influence of DLCP on the flight dynamics of coaxial compound helicopters. The trim features, power consumption, rotor tip clearance, dynamic stability and controllability of the vehicle are discussed. We can draw the conclusions as follows:

(1) To calculate the aerodynamics of coaxial hingeless rotors, an inflow interaction model is proposed based on a revised blade element momentum theory and the wake superposition model. The variation of the interference velocity and area with flight speed are considered in the model. The results of the aircraft flight dynamics model achieve a satisfactory agreement with previous data.

(2) DLCP influences the trim characteristics of the coaxial compound helicopter, especially in low-speed forward flight. A negative DLCP alleviates airflow interactions, and increases thrust from the lower rotor. Thus, fewer collective cyclic pitches and differential collective pitch are required. Variation of the longitudinal stick first increases and then decreases as the interference area moves rearward, thus the negative longitudinal gradient is alleviated. On the other hand, DLCP results in slight lateral and heading control displacements at high speeds. In addition, it reduces the tip clearance throughout the flight range due to the differential pitching moment and higher lower-rotor thrust.

(3) DLCP changes the rotor power consumption at low speeds. The average rotor and total power reduction reach 4.68% and 2.9%, respectively, when DLCP is -3°. As DLCP further decreases, the total power efficiency is degraded by a) the increase in propeller consumption, and b) the unbalanced lift distribution between the coaxial rotor.

(4) The variation of aerodynamic loads and inflow alter the stability of the rotorcraft. A negative DLCP leads to improved phugoid and dutch roll frequencies and heave subsidence due to the reduced interference. In contrast, the pitch and roll subsidences are slightly degraded.

(5) The variation of aerodynamic loads and inflow alter the controllability of the rotorcraft. The control power of the collective pitch has minor reduction and the on-axis lateral derivative is increased. In addition, the control derivates of the differential collective pitch and the longitudinal cyclic pitch vary with speed and DLCP.

(6) In conclusion, DLCP is a good way to improve the low-speed performance of the coaxial compound helicopter and alleviates the mutual interference between coaxial rotors. Meanwhile, it alleviates the negative longitudinal gradient due to severe interaction. Therefore, it can be used to improve the low-speed flight performance of the helicopter, such as takeoff and landing.

Declaration of Competing Interest

The authors declare that they have no known competing financial interests or personal relationships that could have appeared to influence the work reported in this paper.

Acknowledgement

This study was supported by A Project Funded by the Priority Academic Program Development of Jiangsu Higher Education Institutions, China.

References

1. Johnson W. Influence of lift offset on rotorcraft performance. Moffett Field(CA): Ames Research Center; 2009. Report No.: NASA/TP–2009-215404.
2. Yuan Y, Thomson D, Chen RL. Investigation of lift offset on flight dynamics characteristics for coaxial compound helicopters. *J Aircr* 2019;**56**(6):2210–22.
3. Schmaus JH, Chopra I. Aeromechanics of rigid coaxial rotor models for wind-tunnel testing. *J Aircr* 2017;**54**(4):1486–97.
4. Deng JH, Fan F, Liu PA, et al. Aerodynamic characteristics of rigid coaxial rotor by wind tunnel test and numerical calculation. *Chin J Aeronaut* 2019;**32**(3):568–76.
5. Jacobellis G, Gandhi F, Floros M. Using control redundancy for power and vibration reduction on a coaxial rotor helicopter at high speeds. *J Am Helicopter Soc* 2019;**64**(3):1–15.
6. Ruddell AJ. Advancing blade concept (ABCTM) development. Sikorsky: Aircraft Division of United Technologies Corporation; 1981. Report No.: USAAVRADCOM-TR-81-D-5.
7. Ruddell A. *Advancing blade concept/ABC/development test program. 1st flight test conference*; Las Vegas NV, USA. Reston: AIAA; 1981.
8. Walsh D, Weiner S, Arifian K, et al. High airspeed testing of the Sikorsky X2 technology demonstrator. *American helicopter society 67th annual forum*; Virginia Beach, VA. 2011.
9. Eller E. X2^{TM} load alleviating controls. *American helicopter society 68th annual forum*; Fort Worth, TX. 2012.
10. Lorber PF, Law GK, O'Neill JJ. Overview of S-97 RaiderTM scale model tests. *American helicopter society 72th annual forum*; West Palm Beach, Florida, USA. 2016.
11. Lorber PF, Zhao J, Bowles P, et al. S-97 Raider® wake-empennage interaction flight data and correlation. *Vertical flight society (VFS) 77th annual forum & technology display*. 2021.
12. Jia ZQ, Lee S. Impulsive loading noise of a lift-offset coaxial rotor in high-speed forward flight. *AIAA J* 2020;**58**(2):687–701.
13. Chen RL, Yuan Y, Thomson D. A review of mathematical modelling techniques for advanced rotorcraft configurations. *Prog Aerosp Sci* 2021;**120** :100681.
14. Yuan Y, Chen RL, Li P. Trim investigation for coaxial rigid rotor helicopters using an improved aerodynamic interference model. *Aerosp Sci Technol* 2019;**85**:293–304.
15. Ho JC, Yeo H. Analytical study of an isolated coaxial rotor system with lift offset. *Aerosp Sci Technol* 2020;**100** :105818.

16. Makeev PV, Ignatkin YM, Shomov AI. Numerical investigation of full scale coaxial main rotor aerodynamics in hover and vertical descent. *Chin J Aeronaut* 2021;**34**(5):666–83.
17. Zhao JG, He CJ. A finite state dynamic wake model enhanced with vortex particle method–derived modeling parameters for coaxial rotor simulation and analysis. *J Am Helicopter Soc* 2016;**61**(2):1–9.
18. Valkov T. Aerodynamic loads computation on coaxial hingeless helicopter rotors. *28th aerospace sciences meeting*; Reno, NV, USA. Reston: AIAA; 1990.
19. Leishman JG, Ananthan S. Aerodynamic optimization of a coaxial proprotor. *American helicopter society 62th annual forum*; Phoenix, AZ, United States 2006.
20. Lee S, Dassonville M. Iterative blade element momentum theory for a coaxial rotor. *Vertical flight society (VFS) 75th annual forum & technology display*; Philadelphia, Pennsylvania. 2019.
21. Kong YB. Development of a finite state coaxial rotor dynamic inflow model [dissertation]. Atlanta: Georgia Institute of Technology; 2018.
22. Ferguson K, Thomson D. Flight dynamics investigation of compound helicopter configurations. *J Aircr* 2015;**52**(1):156–67.
23. Gaonkar G, Peters D. Review of dynamic inflow modeling for rotorcraft flight dynamics. *27th structures, structural dynamics and materials conference*; San Antonio, TX, USA. Reston: AIAA; 1986.
24. Yan XF, Chen RL. Augmented flight dynamics model for pilot workload evaluation in tilt-rotor aircraft optimal landing procedure after one engine failure. *Chin J Aeronaut* 2019;**32**(1):92–103.
25. Pleasants WA. A rotor technology assessment of the advancing blade concept. Moffett Field(CA):Ames Research Center; 1983. Report No.: NASA-TM-84298.
26. Landgrebe AJ. The wake geometry of a hovering helicopter rotor and its influence on rotor performance. *J Am Helicopter Soc* 1972;**17**(4):3–15.
27. Leishman JG. *Principles of helicopter aerodynamics*. 2nd ed. Cambridge: Cambridge University Press; 2006.
28. Innocenti M. Helicopter flight dynamics: the theory and application of flying qualities and simulation modeling. *J Guid Control Dyn* 1999;**22**(2):383–4.
29. Kim FD. Formulation and validation of high-order mathematical models of helicopter flight dynamics [dissertation]. Maryland: University of Maryland; 1991.
30. Xin H, Zhang C, Black A, et al. S-97 Raider® GENHEL model development and correlation with flight test data. *Vertical flight society 77th annual forum*. 2021.
31. Klingloff RF. Rigid coaxial (ABC) TM rotor system stability and control characteristics. *32nd annual national forum of the Amercian helicopter society*; Washington, D.C. 1976.
32. Felker F. Performance and loads data from a wind tunnel test of a full-scale, coaxial, hingeless rotor helicopter. Moffett Field(CA): Ames Research Center; 1981. Report No.: NASA-TM-81329.
33. Kim HW, Kenyon AR, Brown RE, et al. Interactional aerodynamics and acoustics of a hingeless coaxial helicopter with an auxiliary propeller in forward flight. *Aeronaut J* 2009;**113**(1140):65–78.
34. Yuan Y, Thomson D, Chen RL. Propeller control strategy for coaxial compound helicopters. *Proc Inst Mech Eng Part G J Aerosp Eng* 2019;**233**(10):3775–89.
35. Yuan Y, Thomson D, Chen RL, et al. Heading control strategy assessment for coaxial compound helicopters. *Chin J Aeronaut* 2019;**32**(9):2037–46.
36. Chen RTN. Effects of primary rotor parameters on flapping dynamics. Washington, D.C.: NASA; 1980. Report No.: NASA-TP-1431.